

This is the peer reviewed version of the following article:

Preparation of phosphoric acid-based geopolymer foams using limestone as pore forming agent - Thermal properties by in situ XRPD and Rietveld refinements / Gualtieri, Eva Magdalena; Romagnoli, Marcello; Gualtieri, Alessandro. - In: JOURNAL OF THE EUROPEAN CERAMIC SOCIETY. - ISSN 0955-2219. - 35:11(2015), pp. 3167-3178. [10.1016/j.jeurceramsoc.2015.04.030]

*Terms of use:*

The terms and conditions for the reuse of this version of the manuscript are specified in the publishing policy. For all terms of use and more information see the publisher's website.

16/04/2024 15:59

(Article begins on next page)

1           **PHOSPORIC ACID-BASED GEOPOLYMER FOAMS USING NATURAL LIMESTONE AS PORE**  
2           **FORMING AGENT -THERMAL PROPERTIES BY *IN SITU* XRPD AND RIETVELD REFINEMENTS**

3  
4  
5 Magdalena Lassinantti Gualtieri<sup>a</sup>, Marcello Romagnoli<sup>a</sup>, Alessandro F. Gualtieri

6  
7 *<sup>a</sup>Dipartimento Ingegneria “Enzo Ferrari”, Università di Modena e Reggio Emilia, Via*  
8 *Vignolese 905/a, I-41125 Modena Italy*

9 *<sup>b</sup>Dipartimento di Scienze Chimiche e Geologiche, Università degli studi di Modena e Reggio*  
10 *Emilia, Via S.Eufemia 19I, I-41121 Modena Italy*

11  
12 Corresponding author: Magdalena Lassinantti Gualtieri

13 *Full mail address: Dipartimento Ingegneria “Enzo Ferrari”, Università di Modena e Reggio*  
14 *Emilia, Via Vignolese 905/a, I-41125 Modena Italy*

15 Tel. +39 059 2056282

16 Fax. +39 059 2056243

17 Email: [magdalena.gualtieri@unimore.it](mailto:magdalena.gualtieri@unimore.it)

18  
19 Submitted as RESEARCH PAPER to **Journal of the European Ceramic Society**

20  
21 *Keywords:* Geopolymer; inorganic foam; thermal expansion; phase transformation; X-ray  
22 diffraction

25 ABSTRACT

26 In this work, geopolymer foams were obtained by reacting metakaolin with phosphoric acid  
27 and using natural calcite/dolomite as foaming agent. Total porosity and thermal conductivity  
28 were ca. 70 % and  $0.083 \pm 0.008$  W/mK, respectively. Rietveld refinements, using both *ex-*  
29 and *in situ* XRPD data, were performed in order to elucidate the phase stability of the formed  
30 binder up to 1200 °C. The results showed that the amorphous matrix partially crystallized in  
31 tridymite and cristobalite type structures of  $\text{AlPO}_4\text{-SiO}_2$  solid solutions at about 700 °C. At  
32 1000°C, 3:2 mullite started to crystallize, possibly from unreacted metakaolinite, resulting in  
33 co-crystallization of  $\text{SiO}_2$  cristobalite. At the same time, the amount of tridymite-type  
34 structure decreased, possibly due to selective phase transformation of  $\text{AlPO}_4$  tridymite to  
35 cristobalite, leaving behind the  $\text{SiO}_2$  isostructure. The geopolymer paste composition allows  
36 to tailor the mullite content in the refractory foam.

37

38

39

40

41

42

43

44

45

46

47

48

49

## 50 **1. Introduction**

51 Geopolymers are generally obtained by **treating a reactive aluminosilicate precursor**, such as  
52 metakaolinite or fly ash, with **an** alkaline sodium silicate solution at near-ambient temperature  
53 [1]. The obtained structure is amorphous, consisting of covalently bonded  $[\text{SiO}_4]^{4-}$  and  
54  $[\text{AlO}_4]^{5-}$  tetrahedra in which the net negative charge introduced by the presence of aluminum  
55 is compensated by alkali cations [1]. About a decade ago, Wagh suggested that inorganic  
56 polymers having  $[\text{PO}_4]^{3-}$  in place of  $[\text{SiO}_4]^{4-}$  should be considered as a new class of  
57 geopolymers [2]. Cao et al. used various spectroscopic techniques ( $^{29}\text{Si}$  and  $^{27}\text{Al}$  MAS-NMR,  
58 FTIR) to study metakaolinite before and after reaction with phosphoric acid [3]. Based on the  
59 observed results, the authors claimed that the reaction **occurs** mainly between the phosphate  
60 tetrahedral unit and the Al-O layer in metakaolinite, thus forming a tree-dimensional network  
61 [3]. The model proposed by the authors thus involves metakaolinite particles bonded together  
62 by oxygen-bridged Al and P in tetrahedral coordination [3], which eliminates the need of  
63 extra-framework charge-compensating cations. The material thus acquires new interesting  
64 properties such as low dielectric loss [4].

65 In recent years, **geopolymer foam** has attracted attention from the scientific community due to  
66 high potential as green alternative to conventional foams based on ordinary Portland cement  
67 [5], and as precursor for the production of refractory foams [6, 7].

68 **The techniques used to produce geopolymer foams** are analogous to those **applied** for  
69 conventional foamed concretes [5]; (i) addition of a gas forming agent in the fresh paste [8-  
70 15] (ii) air-entrainment by direct addition of a preformed foam [16]. In scientific studies, the  
71 most common gas **forming agents** are **aluminum powder** [8-11], **metallic silicon (added as**  
72 **fumed silica which contains metallic silicon as impurity)** [12-13] and **hydrogen peroxide** [14,  
73 **15]**. Another interesting technique recently presented as a viable approach for the production  
74 of porous geopolymers is emulsion templating [17,18].

75 In a recent review on geopolymer foam, it was pointed out that the economical/environmental  
76 benefits of geopolymer foam concrete over conventional OPC foam concrete may be  
77 compromised if high dosages of common pore forming agents (i.e. Al powder, fumed silica)  
78 with high embodied energy are used [5]. An alternative to low doses of these expensive  
79 additives may be replacement with other more economically advantageous ones [5]. Common  
80 pore forming agents for the preparation of metal foams [19] and glass foams [20] are  
81 carbonates. When the carbonate-containing melts are exposed to temperatures higher than the  
82 decomposition temperature of the carbonates, CO<sub>2</sub> evolves and gives rise to a porous  
83 structure. The pore forming action of these compounds can also rely on chemical  
84 decomposition at near-ambient temperature, for example when used for the preparation of  
85 porous metal phosphate ceramics [21, 22].

86 Limited work has been aimed to study the phase evolution of phosphorus-based geopolymers  
87 [23]. Liu et al. studied the high-temperature behavior of geopolymers obtained by reaction  
88 between a pure aluminosilicate and phosphoric acid [23]. The results obtained for the  
89 chemically pure starting material in that work are perhaps not comparable to results obtained  
90 for geopolymers prepared using conventional raw materials such as metakaolin.

91 In this work, inorganic foams were prepared by reaction of metakaolin with phosphoric acid  
92 using natural limestone as pore forming agent. The amount of foaming agent was kept fixed  
93 while the molar composition of the paste was varied. The changes in mineralogical  
94 composition, effective thermal conductivity ( $\lambda_{\text{eff}}$ ) and total porosity of the foams following  
95 exposure to high temperatures (800-1000°C) were determined. In addition, special emphasis  
96 was paid to the phase evolution of the as-synthesized geopolymers. The proposed method is  
97 promising for the preparation of inorganic insulation material at near-ambient temperatures  
98 with may be transformed into an aluminum phosphate/mullite ceramic with tailored phase  
99 composition for high-temperature applications.

100

## 101 2. Experimental

### 102 2.1. Sample preparation

103

104 The procedure for **the** preparation of fumed geopolymer concrete was as follows: The desired  
105 proportions of industrial metakaolin (MK, Sibelco, Italy), orthophosphoric acid (85%, Carlo  
106 Erba) and double-distilled water were carefully mixed to obtain a homogeneous base paste.

107 Following homogenization, a fixed amount of a liquid nonionic surfactant (Marlipal) was

108 added (0.16 grams per 100 g of MK). Subsequently, a limestone slurry was rapidly mixed

109 with the paste resulting in expansion. This slurry was prepared in a previous step by

110 dispersing **lime**stone powder in a part of the desired water content of the base paste

111 composition. To increase disaggregation, a small amount of deflocculant

112 (Hexametaphosphate, Carlo Erba) was also added. The amount of limestone was 4 g for each

113 100 g of MK. A total of 13 different pastes were prepared according to an experimental plan

114 generated by the software Design-Expert v. 6.0.10 (Stat-ease Inc) in which the factors wt.%

115 deflocculant, MK/water ratio and MK/H<sub>3</sub>PO<sub>4</sub> ratio were varied in the ranges 0-0.5, 1.19-1.39

116 and 2.02-3.75, respectively. The deflocculant used for the limestone slurry was also included

117 **as a variable** in order to assure that this additive did not affect the technological **properties** of

118 the hardened material. The investigated compositions are shown in Table 1.

119 The expanding geopolymer pastes were directly cast in cylindrical (height 12 cm, diameter

120 3.76 cm) polyethylene molds, three for each investigated composition. A lubricated **polymer**

121 rod was inserted in the center of each cylinder in order to create a hole which served to

122 accommodate the sensor for thermal conductivity ( $\lambda_{\text{eff}}$ ) measurements that will be described

123 later. The filled molds were left at ambient temperature for about 1h after which they were

124 sealed and put in an electrical furnace holding a temperature of 60 °C. After 24 h, the sealed

125 molds were left at ambient temperature for 28 days. Following curing, the samples were

126 extracted from the molds, dried at 80 °C for 96 h and consequently kept in a dessicator prior  
127 to further treatment.

128

## 129 **2.2. Analysis techniques**

130 The chemical composition of metakaolin was determined by X-ray fluorescence spectroscopy  
131 (XRF, Philips PW 1480).

132 The BET specific surface area of the raw materials was measured using a Gemini 2360  
133 (Micromeritics) instrument. Nitrogen (high purity grade) was used as probe gas.

134 The grain size distribution of the limestone used as pore forming agent was determined using  
135 a laser granulometer (Mastersizer 2000, Malvern Instruments) equipped with a system for  
136 measurement in humid (Hydro 2000S). Deionized water was used as carrier fluid.

137 Calcimetry (Dietrich-Fruhling apparatus) was used to determine the carbonate content in the  
138 limestone.

139 The bulk densities ( $\rho$ ) of dry geopolymer specimens were determined by weight and  
140 geometrical calculations of dry samples (24 h at 105 °C).

141 The true densities ( $\rho_t$ ) were determined using a gas displacement pycnometer (AccuPyc 1330,  
142 Micromeritics Inc., USA). Samples were ground to fine powders and consequently dried (24h  
143 at 105 °C) prior to analyses.

144 The total porosity ( $TP$ , %) was calculated according to [24]:

145

$$146 \quad TP = \left( 1 - \frac{\rho}{\rho_t} \right) \cdot 100 \quad (2)$$

147

148 Scanning electron microscopy (SEM) analyses were performed using an environmental SEM  
149 (ESEM Quanta-200, FEI company) equipped with a INCA-350 (Oxford Instruments) energy-

150 dispersive X-ray spectroscopy analysis system. For SEM analyses, polished cross-sections of  
151 hardened geopolymers were prepared as follows: In the first step, each sample was  
152 impregnated with epoxy resin. Following hardening of the resin, sequential rough polishing  
153 was performed using 240-2000 mesh grade SiC abrasive paper. In the last step, mirror finish  
154 was accomplished using 2.5 and 0.5  $\mu\text{m}$  diamond pastes. The polished samples were  
155 consequently washed in acetone and dried at 40 °C. The washed and dried samples were  
156 mounted on aluminum stubs gold coated (10 nm) prior to electron microscopy observations.  
157 Transmission electron microscopy analyses (TEM) were performed on ceramic foams using a  
158 Jeol JEM 2010 instrument working at 200 kV. The foams were gently crushed and the  
159 resulting powder was dispersed in distilled water. Following ultrasonification for ca. 1h,  
160 particles were collected on a Cu grid sample holder and dried.

161 Simultaneous thermal analyses (TG/DTA) were performed in air (Pt crucible, 20 °C/min  
162 heating rate up to 1400 °C) using a STA 429 CD instrument (Netzsch, Geraetebau GmbH,  
163 Germany).

164 X-ray powder diffraction (XRPD) data were collected using a  $\theta/\theta$  diffractometer  
165 (PANalytical,  $\text{CuK}\alpha$  radiation), equipped with an Anton Paar HTK 16 resistance heating  
166 chamber. A real time multiple strip (RTMS) detector allowed fast data acquisition. The  
167 incident beam pathway included a soller slit (0.04 rad) as well as divergence and anti-  
168 scattering slits. These slits had an opening of 0.5°. The pathway of the diffracted beam  
169 included a Ni filter, a soller slit (0.04 rad) and an antiscatter blade (5 mm). A virtual step scan  
170 (0.0167 °2 $\theta$ ) was performed in the range 3-90 °2 $\theta$ .

171 Samples for *ex-situ* data collection were carefully ground and mounted in aluminium sample  
172 holders using side-loading.

173 *In situ* data were collected for both cured geopolymer sample (composition 3 in Table 1) and  
174 heat-treated (800 °C and 1000°C) counterparts. The temperature on the heating strip,  
175 functioning as sample holder, was calibrated against known phase transitions and phase

176 decompositions. All experiments were performed in air using a heating rate of 20 °/min. For  
177 as-synthesized and cured samples, data were collected in the range 15-50 °2 $\theta$  using an  
178 acquisition time of 3 min. Instead, data for heat-treated samples were collected in the range  
179 15-65 °2 $\theta$  using an acquisition time of about 11 min. The faster data collection in the former  
180 case was chosen to more closely mimic the continuous heating ramp applied in the TG/DTA  
181 analyses of the same sample.

182 Full quantitative phase analyses were performed using XRPD data and Rietveld refinements.  
183 The software used were GSAS [25] and its graphical interface EXPGUI [26]. The refinement  
184 strategy was adopted from previous work, including calibration of instrumental and profile  
185 parameters [27]. Samples for FQPA were mixed with a known amount of internal standard  
186 (10 wt% corundum NIST 676a) which was treated as part of the sample in subsequent  
187 Rietveld refinement analyses. Elaboration of data extracted from Rietveld refinements was  
188 performed according to the procedures previously described in detail [28].

189 Accurate unit cell parameters of the constituting crystalline phases could be followed in  
190 temperature (*in situ* data) by using a standard silicon powder (NIST 640c) directly mixed in  
191 the sample. The correct unit cell of the Si standard at each temperature, calculated using the  
192 certified unit cell at RT and known thermal expansion [29], was fixed in the Rietveld  
193 refinements in order to correct for zero offset as well as sample displacement due to thermal  
194 expansion of the sample holder. The structure models of the main phases used for the  
195 refinements were:  $\alpha$ -Al<sub>2</sub>O<sub>3</sub> [30]; triclinic low-tridymite structure in space group *F1* [31];  
196 tetragonal low-cristobalite structure in space group *P4<sub>1</sub>2<sub>1</sub>2* [32], cubic high-cristobalite in  
197 spacegroup *Fd-3m* [33]; low-quartz in space group *P3<sub>2</sub>21* [34], mullite in spacegroup *Pbam*  
198 [35]. Tridymite present in calcined samples at RT fits well with the triclinic structure (space  
199 group *F1*) described by Graetsch [31]. However, already at 113 °C, the 240 peak present at  
200 about 27.2 °2 $\theta$  disappears, indicating a phase transition to higher symmetry. It is well-known  
201 that the tridymite structure displays a sequence of phase transitions during heating [36,37,38].

202 However, for sake of simplicity and difficulty to identify the various temperature-induced  
203 modifications, tridymite was refined in space group *F1* at all investigated temperatures.  
204 Mercury porosimetry data were collected using an Autopore IV 9500 scanning mercury  
205 porosimeter (maximum pressure 33000 psia, pore size range 0.005-360 $\mu$ m). The contact angle  
206 and surface tension of mercury were set at 130° and 485 dynes/cm, respectively. Prior to  
207 analyses, samples were dried at 110 °C for 24 h and consequently kept in a dessicator.  
208 Effective thermal conductivity ( $\lambda_{\text{eff}}$ ) measurements at 28 °C were performed using a KD2 Pro  
209 Thermal properties analyzer (Decagon Devices, Inc) equipped with a TR-1 sensor needle.  
210 Thermal grease was used to reduce contact resistance between the sensor and the material.

211

### 212 **3. Results and Discussions**

#### 213 **3.1 General characterization of the starting material**

214 Figure 1 shows the XRD patterns for metakaolin used as raw material for sample preparation  
215 (a) as well as the natural limestone used as pore forming agent (b). The metakaolin exhibits  
216 the typical background bump associated with metakaolinite [39] and contains quartz,  
217 muscovite/illite and microcline as minor crystalline phases. FQPA results obtained using an  
218 internal standard and the Rietveld method (see experimental) are shown in Table 2, together  
219 with results from chemical analysis. Although some degree of long-range order is preserved  
220 in metakaolinite [39], it is reasonable to treat this phase as being completely amorphous in the  
221 FQPA. As shown in Table 2, the amorphous content in the metakaolin amounts to 82 wt.%,  
222 most probably assigned to the metakaolinite content.

223 The natural limestone used as pore forming agent contains calcite and dolomite with a trace  
224 amount of quartz. Semi-quantitative phase analysis with XRPD data (see Figure 1) and the  
225 Rietveld method gave the following mineralogical composition:  $14.1 \pm 0.1$  Wt.% dolomite;

226  $85.4 \pm 0.1$ Wt.% calcite;  $0.5 \pm 0.1$  Wt.% quartz. The amount of carbonates is in good  
227 agreement with the calcimetry results that gave a total carbonate content of 99 Wt.%.  
228 The grain size distribution of metakaolin, determined by laser diffraction showed D(50) and  
229 D(90) was  $2.8 \mu\text{m}$  and  $8.3 \mu\text{m}$ , respectively. The corresponding values for the natural  
230 limestone was  $5.3 \mu\text{m}$  and  $16.7 \mu\text{m}$ .

231

## 232 **3.2. Macroscopic properties of inorganic foams**

233

### 234 *3.2.1 Geopolymer foams*

235 Table 3 shows the results from the various measurements performed on the hardened and  
236 dried samples ( $\rho_t$ =true density,  $\rho$ =bulk density, TP=total porosity,  $\lambda_{\text{eff}}$  =effective thermal  
237 conductivity). The porosity range of the samples obtained from the different compositions is  
238 very narrow, being 69-76 %. As a consequence, the  $\lambda_{\text{eff}}$  range is also narrow (0.07-0.09  
239 W/mK). No statistically relevant correlations could be found between the independent  
240 parameters and the macroscopic properties of the resulting samples. Controlled addition of the  
241 pore forming agent is generally used to tailor the porosity created in the hardened matrix [8].  
242 In the work presented here, the weight ratio MK/limestone was kept fixed and low enough to  
243 guarantee bubble saturation of the fresh paste. Hence, the obtained porosity probably  
244 represent the upper limit at which a continuous solid skeleton is formed.

245 Figure 2 shows low-magnification BSE images of polished cross-sections of two typical  
246 samples representing the general distribution of the macroporosity created by the pore  
247 forming agent. The selected magnification allows to quantify pores in the approximate size  
248 range  $100\text{-}3000 \mu\text{m}$ . Although difficult to evaluate, it appears that the porous structure was  
249 created by coalesced gas bubbles, leading to high pore interconnectivity in the hardened  
250 structure. Some samples display large round-shaped pores (for example sample 10 displayed

251 in Figure 2a) whereas other samples have smaller interconnected pores (for example sample 3  
252 in Figure 2b). Image analyses using the free-ware ImageJ [40] of five representative BSE  
253 images of each sample were performed. The mean value of the Feret's diameter for sample 3  
254 and 10 was found to be 0.46 and 0.55 mm, respectively. The size distribution of pores smaller  
255 than the ones observable in the BSE images in Figure 2 were determined by mercury  
256 intrusion experiments and will be discussed later (section 3.2.2.).

257 Qualitative analyses of the as-prepared samples (not shown here) evidenced an important  
258 background signal in all diffractograms, indicative of amorphous material. In fact, similar to  
259 alkali-activated metakaolinite, lack of long-range order is expected in geopolymeric material  
260 obtained from reaction between metakaolinite and phosphoric acid [3]. Crystalline phases  
261 include quartz and muscovite/illite, already present in the metakaolin used as raw material  
262 (see Table 2), and newly-formed tridymite-type structure in some samples. As an example,  
263 FQPA of sample 3 was performed and the following weight composition was obtained: quartz  
264  $9.3 \pm 0.1$ ; tridymite-type structure  $1.5 \pm 0.2$ ; muscovite/illite  $2.7 \pm 0.2$ ; amorphous  $86.5 \pm 0.2$ . The  
265 Rietveld refinement output is shown in Figure 3 where the observed, calculated and difference  
266 curves are depicted.

267

### 268 3.2.2. Ceramic foams by firing of geopolymer precursor foam

269 Figure 4 shows the true density (a), bulk density (b), total porosity (c) and effective thermal  
270 conductivity (d) of the heat-treated samples as a function of the corresponding values for the  
271 as-prepared samples. It should be pointed out that only one sample for each batch was heat-  
272 treated and the data shown in Figure 4 corresponds to the exact values obtained for that  
273 sample before and after heat-treatment.

274 Without exceptions, the true density apparently increased following heat-treatment, probably  
275 due to crystallization of the amorphous phase into a more dense structure. Generally speaking,  
276 the bulk density also increased with the exception of a couple of points at the high and low

277 density-regions of the curve (Figure 4b). Heating at 1000 °C resulted in a structure with  
278 higher total porosity (see Figure 4c) and up to threefold higher  $\lambda_{\text{eff}}$  (see Figure 4d). Although  
279 increased porosity accompanied with higher  $\lambda_{\text{eff}}$  could be considered a paradox, the results are  
280 surely explained by densification of the solid skeleton.

281 Mercury intrusion experiments were performed to evaluate the heat-induced changes of the  
282 porous network for samples having compositions 3 and 10, showing different types of  
283 macropores in the as-prepared state (see BSE images in Figure 2). The total intrusion volume  
284 before and after calcination for sample 3 was 0.4486 and 0.4797 mL/g, respectively. The  
285 corresponding values for sample 10 were 0.5554 and 0.5615 mL/g. The porosity of sample 3  
286 increased from 49.79 to 51.53 % following calcination. An increase in porosity, from 55.17 to  
287 57.40 %, was also observed for sample 10. Generally speaking, the porosity values are lower  
288 than the ones determined by eq. 2 (compare with data reported in Figure 4c). This is possibly  
289 explained by the presence of closed porosity (thus not accessible to mercury) and/or pores  
290 having sizes out of the measurement range of the instrument (i.e. 0.005-360  $\mu\text{m}$ ). In fact, most  
291 macropores observed in the low-magnification SEM images depicted in Figure 2, are too  
292 large to be evaluated. Nevertheless, the increase in porosity following calcination observed in  
293 the data plotted in Figure 4c is confirmed. Figures 5a and 5b show  $dV/d\log D$  ( $V$  =volume of  
294 intruded mercury) and the cumulative pore volume as a function of pore diameter ( $D$ ), for  
295 sample 3 and 10, respectively. The pore size was calculated using the classical Washburn  
296 equation [41]. Data from both as-prepared and calcined samples are depicted. The pore size  
297 distribution is bimodal, having peaks at about 0.1-0.3  $\mu\text{m}$  and 120-140  $\mu\text{m}$ . The larger pores,  
298 also detectible in the BSE images displayed in Figure 2, were probably created by the  
299 poreforming agent. The smaller macro/meso pores are most probably associated with the  
300 geopolymer phase, although larger than the ones normally observed for alkali-activated  
301 metakaolin [8]. In fact, the mean size of gel pores in inorganic cements obtained by  
302 geopolymerization of metakaolin in an alkaline environment is generally in the meso-pore  
303 range [8]. The lack of fine pores in phosphate geopolymers obtained from laterite was also  
304 recently reported [42]. The most important change in the porous network after calcination is  
305 observed in the small pores. In fact, a shift towards higher values are observed for both  
306 samples. This is not surprising as the geopolymer phase exhibits important mineralogical  
307 changes following calcination, as will be discussed below.

308 Table 4 and Table 5 show the FQPA results and the results from chemical analyses,  
309 respectively, of each composition following calcination at 1000 °C for 3h. As can be observed  
310 from table 4, newly-formed phases are tridymite, cristobalite and mullite. Small amounts of  
311 whitlockite could also be detected, surely originating from the reaction between phosphoric  
312 acid and the pore forming agent (natural limestone). No statistically relevant correlations  
313 could be found between the independent parameters and the macroscopic properties of the  
314 resulting samples, a part from a clear positive linear trend between the amount of formed  
315 mullite and the MK/acid ratio. **Consequently, a liner trend was also found between mullite**  
316 **and the amount of P<sub>2</sub>O<sub>5</sub> from the chemical analyses.** The increased mullite content with  
317 decreasing amount of phosphoric acid is probably related to less reacted metakaolinite which  
318 consequently is available for mullite crystallization. It is thus possible to tailor the amount of  
319 mullite in the calcined material by adjusting the composition of the initial geopolymer paste.  
320 AlPO<sub>4</sub> is isomorphous with silica and may crystallize in its various polymorphos (quartz,  
321 tridymite, cristobalite). It is difficult to distinguish the different isomorphs due to highly  
322 similar powder diffraction patterns. The chemical compositions were calculated based on  
323 stoichiometric formula and the FQPA results presented in Table 4, assuming crystallization of  
324 AlPO<sub>4</sub> cristobalite and tridymite, and compared to the XRF analyses (Table 5). It was found  
325 that the amounts of Al<sub>2</sub>O<sub>3</sub> and P<sub>2</sub>O<sub>5</sub> were severely overestimated, indicating that the  
326 cristobalite and/or tridymite also appears as silica and/or solid solutions of the two  
327 isostructures. Considering the model for geopolymerization of metakaolinite by reaction with  
328 phosphoric acid suggested by Cao et al. [3] (see introduction), the proposed structure indeed  
329 results in a blend of Al, P and Si on a molecular level. Hence, crystallization of solid solutions  
330 of the two isomorphs is possible. In order to elucidate the thermal behaviour of the  
331 geopolymer phase, TG/DTA analyses and an extensive XRPD investigation were conducted.  
332 **The results of these analyses will be discussed in the following section.**

333

### 334 3.3. Thermal phase transformations/transitions

335 Figure 6 shows the results of the thermogravimetric analysis of a powder specimen obtained  
336 from a sample having composition 3 (see Table 1). A significant weight loss (ca. 14.4 %),  
337 accompanied by a broad endothermic DTA peak at 154 °C, was observed in the temperature  
338 range 25-300 °C and assigned to dehydration. The second thermal event, observed at 694 °C,  
339 is exothermic and assigned to crystallization of the amorphous matrix into cristobalite and  
340 tridymite-type structures (see below). Another exothermic peak is observed at 1004 °C,  
341 assigned to mullite crystallization (see below). Figure 7 shows *in-situ* XRPD data (650-960  
342 °C) collected for the same sample and results from quantitative phase analyses using the  
343 known amount of intrinsic quartz as internal standard. As can be observed, tridymite- and  
344 cristobalite-type structures simultaneously crystallize from the amorphous phase already at  
345 the first investigated data point (650 °C). No further increase in quantity of these phases is  
346 observed above 720 °C. It is thus probable that the exothermic reaction observed at 694 °C in  
347 the DTA trace (Figure 6) is due to the simultaneous crystallization of tridymite-type and  
348 cristobalite-type structures.

349 Figure 8 shows *ex-situ* XRPD diffraction patterns collected from sample 3 (same as above)  
350 following calcination for 3 h at three different temperatures (800, 900 and 1000 °C). The  
351 identified phases, apart from quartz already present in the starting material, are tridymite-and  
352 cristobalite-type structures as well as mullite, the latter not appearing until a temperature of  
353 1000 °C is reached. Figure 9 shows the FQPA results of the major constituting phases as a  
354 function of calcination temperature. For comparison, the results of the as-prepared sample is  
355 also displayed. As can be observed, the amounts of tridymite- and cristobalite-type structures  
356 increase up to 900 °C on the expense of the amorphous phase which decreases. At 1000°C,  
357 mullite starts to crystallize. The amount of cristobalite-type structure drastically increases  
358 from 12±0.2 to 32.3±0.5 wt% whereas the opposite is observed for tridymite-type structure  
359 (from 38.5±0.5 to 24.9±0.5 wt%) and amorphous phase (from 40.0±0.6 to 21.2±0.9 wt%). In

360 order to explain these results, the chemical composition of mullite is needed and can be  
361 determined by the unit cell parameters accurately determined in this work. Mullite is a solid  
362 solution of alumina and silica with stoichiometries ranging from  $3\text{Al}_2\text{O}_3:2\text{SiO}_2$  (3:2 mullite)  
363 to  $2\text{Al}_2\text{O}_3:\text{SiO}_2$  (2:1 mullite) [43]. According to Ban and Okada [44], the stoichiometry is  
364 related to the length of the  $a$ -axis (nm) according to the following empirical expression:  
365 
$$\text{Al}_2\text{O}_3 \text{ (mol\%)} = 1443 \times a - 1028.06$$
  
366 Applying this relationship to the sample investigated here gave  $61.3 \pm 0.9$  mol%  $\text{Al}_2\text{O}_3$ .  
367 Hence, the mullite crystallized in the system studied here is close to the high-silica extreme  
368 (i.e. 3:2 mullite). Stoichiometric calculations show that crystallization of 13.3 wt.% 3:2  
369 mullite from metakaolinite results in a 20.8 wt.% decrease in amorphous content and a 7.5  
370 wt.% increase in silica. The expected decrease in amorphous content is thus in rather good  
371 agreement with the observed one (18.8 wt.%, see Figure 9). The increase in cristobalite  
372 content of 20.3 % is explained by co-crystallization with mullite (7.5 wt%) and  
373 recrystallization of tridymite-structure to cristobalite-type structure (13.6 wt.%, see Figure 9).  
374 If this assumption is correct, the cristobalite-type phase present following high-temperature  
375 treatment at  $1000^\circ\text{C}$  should, a part from the  $\text{AlPO}_4:\text{SiO}_2$  cristobalite solid solution, also  
376 include the pure  $\text{SiO}_2$  isostructure. A possible way to investigate this further is to compare the  
377 unit cell volume as a function of temperature for the same sample treated at  $1000^\circ\text{C}$  and  $800^\circ\text{C}$ .  
378 In the latter case, the amount of silica cristobalite should be minor with respect to the one  
379 obtained after calcination at  $1000^\circ\text{C}$ . According to the literature, such changes should result  
380 in important effects on the unit cell dimensions. In fact, the unit cell volume of silica  
381 cristobalite is smaller than the one found for  $\text{AlPO}_4$  cristobalite [45,46].  
382 Figure 10a shows the unit cell volume as a function of temperature for cristobalite. For  
383 comparison, data for solid solutions in the cristobalite system  $\text{AlPO}_4\text{-SiO}_2$  determined by  
384 Horn and Hummel [47] are also shown together with the corresponding curves for the pure  
385 extremes determined by Wright and Leadbetter [48]. First of all, phase transitions are usually

386 accompanied by a change in volume. In fact, the phase transition from  $\alpha$ - to  $\beta$ -cristobalite is  
387 evident in the X-ray powder patterns mainly due to a sudden peak shift to lower  $2\theta$ . In this  
388 work, this change was observed already at 113 °C (see Figure 10a), which is considerably  
389 lower than the transition temperature normally observed for pure silica structures (200-275 °C  
390 [49]). Considering the low chemical purity of the system under study, containing both  
391 alkaline and alkaline earth metals as well as phosphate, incorporation of e.g. Na and Ca as  
392 well as  $\text{AlPO}_4$  in the framework structure is expected and known to affect the transition  
393 temperature and even stabilize  $\beta$ -cristobalite at RT [50]. According to Horn and Hummel  
394 [47], the thermal expansion curves of  $\text{SiO}_2$  and  $\text{AlPO}_4$  cristobalite are not much affected by  
395 the inclusion of  $\text{AlPO}_4$  and  $\text{SiO}_2$  in the respective phase (see Figure 10a). Interestingly, the  
396 curve determined for a sample precalcined at 1000 °C lies between the  $\text{AlPO}_4$  and  $\text{SiO}_2$   
397 extreme, whereas the sample precalcined at 800 °C is close to the  $\text{AlPO}_4/\text{AlPO}_4\text{-SiO}_2$   
398 cristobalite structures (see Figure 10a). The most probable explanation is that the two  
399 cristobalite structures are **exsolved, resulting** in a unit cell volume vs. temperature curve that  
400 represents an average of the unit cell volume of the two phases.

401 Figure 10b shows the unit cell volume as a function of temperature for tridymite and quartz.  
402 In contrast to cristobalite, tridymite exhibits several phase transition with only very small  
403 changes in unit cell volume and therefore difficult to identify by thermal expansion curves  
404 [37]. Nevertheless, the phase transition from orthorhombic to hexagonal structure is rather  
405 clearly identified by a sudden change in thermal expansion [36, 37, 50], which in this work  
406 was observed at about 160 °C, see Figure 10b. Again the much lower phase transition  
407 temperature observed in this work, compared to pure silica tridymite (ca 350 °C [37, 51]) is  
408 not surprising as the transition temperatures are shifted to lower values for  $\text{AlPO}_4$  tridymite.  
409 In addition, the thermal behaviour of tridymite is sensitive to structural defects such as  
410 stacking faults and interstitial cations in the framework [37]. The transition from  $\alpha$ -quartz to

411  $\beta$ -quartz is evident in Figure 10b as a sudden change in thermal expansion and is known to  
412 occur at a temperature of 573 °C [52]. From Figure 10b, it can be observed that the only  
413 difference between the tridymite unit cell volume vs. temperature curves collected for a  
414 sample annealed at 800 °C and 1000 °C is that the latter is shifted to lower values. A possible  
415 explanation, though needing further supporting evidence, is recrystallization of  $\text{AlPO}_4$   
416 tridymite to cristobalite at temperatures higher than 1000 °C, leaving behind a structure  
417 enriched in silica with a smaller unit cell. The thermal expansion of quartz remain practically  
418 invariant as expected (see Figure 10b), indicating a correct analysis.

419 Supporting evidence for the events described above were sought in TEM analyses. Figure 11  
420 shows images of sample 3 (same as above) following calcination at 1000 °C. Thin hexagonal  
421 platelets of tridymite were identified (indicated with A). Round-shaped particles (indicated by  
422 B) composed of Al, P and Si were observed, the molar ratio of the two former elements being  
423 1 indicating an  $\text{AlPO}_4$  phase. P-depleted thin flakes with a granular surface are observed  
424 (indicated with C) and are possibly  $\text{SiO}_2$ -rich tridymite relicts left behind following  
425 recrystallization of  $\text{AlPO}_4$  tridymite to cristobalite as suggested from the thermal expansion  
426 curves discussed above (see Figure 10b). Needle-shaped mullite crystals, indicated by D in  
427 Figure 11d, were observed.

428 In light of the results presented above, the following model for thermal phase evolution of  
429 geopolymers based on metakaolinite and phosphoric acid is proposed: Upon heating, the  
430 amorphous geopolymer crystallizes into tridymite-type and cristobalite-type structures,  
431 resulting in an exothermic DTA peak at 690 °C. The formed structures at this temperature are  
432 most likely solid solutions of  $\text{AlPO}_4$  and  $\text{SiO}_2$  since the calculated chemical composition  
433 based on the FQPA results assuming pure  $\text{AlPO}_4$  phases results in an overestimation of  $\text{P}_2\text{O}_5$   
434 compared to the XRF chemical analyses. This assumption is further supported by the fact that  
435 the unit cell volume vs. temperature curve of cristobalite is close to literature values of  
436  $\text{AlPO}_4$ - $\text{SiO}_2$  solid solutions. When higher temperatures are reached (>1000 °C), the

437 cristobalite content drastically increases due to thermal transformation of unreacted  
438 metakaolinite to 3:2 mullite, thus releasing residual silica. Hence, the cristobalite structure at  
439 this temperature is a mixture of  $\text{AlPO}_4\text{-SiO}_2$  solid solution and the pure  $\text{SiO}_2$  isostructure.  
440 This conclusion is again based on the unit cell vs. temperature curve which in this case is  
441 positioned between the one expected for  $\text{AlPO}_4\text{-SiO}_2$  solid solutions and the pure  $\text{SiO}_2$   
442 structure. Instead, the amount of tridymite-type structure decreases following calcination at  
443 1000 °C. This is possibly explained by selective phase transformation of  $\text{AlPO}_4$  tridymite to  
444 cristobalite leaving behind the  $\text{SiO}_2$  isostructure. In fact, the unit cell volume vs. temperature  
445 curve is shifted to lower values with respect to a sample calcined at lower temperature  
446 (800°C).

447 Liu et al. studied the high-temperature behavior of geopolymers obtained by reaction of a  
448 pure aluminosilicate and phosphoric acid [10]. Qualitative evaluations of XRD patterns  
449 collected from fired samples showed that the amorphous geopolymer started to crystallize at  
450 900 °C, thus forming quartz and berlinite. At higher temperatures (>1150 °C), cristobalite and  
451 mullite crystallized. In addition, orthorhombic aluminum phosphate also appeared. The  
452 important differences observed in phase evolution between the samples studied by Liu et al.  
453 and the ones studied in the present work demonstrate that phase stability and thermal  
454 transformations in phosphate geopolymers may differ depending on the starting material. In  
455 particular, the chemical composition (possible atomic substitutions which might stabilize  
456 metastable structures) and chemical homogeneity (e.g degree of geopolymerization, linking of  
457 tetrahedral units) are surely important.

458

#### 459 **4. Conclusions**

460 In this work, natural limestone was used as pore forming agent in the preparation of foamed  
461 geopolymer with high porosity (68-70%) and low thermal conductivity (0.092-0.095 W/mK).  
462 The adopted synthesis approach included activation of metakaolinite with phosphoric acid,

463 leading to an amorphous binder phase. The acidic environment of the fresh paste provoked  
464 chemical decomposition of added carbonates with gas release (CO<sub>2</sub>) and consequent foam  
465 formation. Thermal and microstructural properties were investigated to shed light on the  
466 chemico-physical nature of the foamed geopolymer. In particular, *in situ* XRPD and Rietveld  
467 refinements gave accurate thermal expansion curves and quantitative phase analysis data of  
468 the constituting phases. Following firing at 1000 °C, the total porosity slightly increased  
469 whereas  $\lambda_{\text{eff}}$  more than doubled due to partial crystallization and consequent densification of  
470 the solid skeleton. The hardened amorphous structure partially crystallized in tridymite-type  
471 and cristobalite-type AlPO<sub>4</sub>-SiO<sub>2</sub> solid solutions at a temperature of about 700 °C. At 1000  
472 °C, mullite started to crystallize, probably from non-reacted metakaolinite leading to  
473 crystallization of residual SiO<sub>2</sub> to cristobalite. In concomitance with this event, phase  
474 transformation of AlPO<sub>4</sub> tridymite-type to cristobalite-type structure likely occurred, leaving  
475 behind the SiO<sub>2</sub> tridymite isostructure. The carbonate, present in amorphous form in the non-  
476 heated geopolymer, crystallized into  $\beta$ -Ca<sub>3</sub>PO<sub>4</sub>.

477

## 478 **Acknowledgements**

479

480 The authors are thankful to V. Ghidoni for assistance during sample preparation. P. Miselli is  
481 kindly acknowledged for performing the thermal analysis. Valuable help with electron  
482 microscopy analyses were provided by E. Fabbri. and M. Zapparoli.

483

## 484 **References**

- 485 [1] Duxson P, Fernández-Jiménez A, Provis JL, Lukey GC, Palomo A, van Deventer JSJ.  
486 Geopolymer technology: the current state of the art. *J Mater Sci* 2007;**42**: 2917–33.

- 487 [2] Wagh AS. Chemically bonded phosphate ceramics-A novel class of geopolymers. *Ceram*  
488 *Trans* 2005; **165**: 107-16.
- 489 [3] Cao D, Su D, Lu B, Yang Y. Synthesis and structure characterization of geopolymeric  
490 material based on metakaolinite and phosphoric acid. *J Chin Ceram Soc* 2005; **33**: 1385-  
491 89.
- 492 [4] Cui X, Ping L, He Y, Chen J, Zhou J. A novel aluminosilicate geopolymer material with  
493 low dielectric loss. *Mater Chem and Phys* 2011; **130**: 1-4.
- 494 [5] Zhang Z, Provis JL, Reid A, Wang H. Geopolymer foam concrete: An emerging material  
495 for sustainable construction. *Constr Build Mater* 2014; **56**: 113-27.
- 496 [6] Kuenzel C, Grover LM, Vandeperre L, Boccaccini AR, Cheeseman CR. Production of  
497 nepheline/quartz ceramics from geopolymer mortars. *J Eur Ceram Soci* 2013; **33**: 251-8.
- 498 [7] He P, Jia D, Wang S. Microstructure and integrity of leucite ceramics derived from  
499 potassium-based geopolymer precursor. *J Eur Ceram Soc* 2013; **33**: 689-98.
- 500 [8] Kamseu E, Nait-Ali B, Bignozzi MC, Leonelli C, Rossignol S, Smith DS, Bulk  
501 composition and microstructure dependence of effective thermal conductivity of porous  
502 inorganic polymer cements. *J Eur Ceram Soc* 2012; **32**: 1593-603.
- 503 [9] Arellano Aguilar R, Burciaga Díaz O, Escalante García JI. Lightweight concretes of  
504 activated metakaolin-fly ash binders, with blast furnace slag aggregates. *Constr Build*  
505 *Mater* 2010; **24**: 1166-75.
- 506 [10] Liu LP, Cui XM, Qiu SH, Yu JL, Zhang L. Preparation of phosphoric acid-based porous  
507 geopolymers. *Appl Clay Sci* 2010; **50**: 600-3.
- 508 [11] Bell JL, Kriven WM. Preparation of ceramic foams from metakaolin-based geopolymer  
509 gels. *Ceram Eng Sci Proc* 2009; **29**: 97-111.
- 510 [12] Landi E, Medri V, Papa E, Dedeczek J, Klein P, Benito P, Vaccari A. Alkali-bonded  
511 ceramics with hierarchical tailored porosity. *Appl Clay Sci* 2013; **73**: 56-64.

- 512 [13] Prud'homme E, Michaud P, Joussein E, Peyratout C, Smith A, Rossignol S. In situ  
513 inorganic foams prepared from various clays at low temperature. *Appl Clay Sci* 2011;  
514 **51**: 15-22.
- 515 [14] Shiu H-S, Lin K-L, Chao S-J, Hwang C-L, Cheng T-W. Effects of foam agent on  
516 characteristics of thin-film transistor liquid crystal display waste glass-metakaolin-based  
517 cellular geopolymer. *Environ Prog Sustain Energy* 2014; 33: 538-50.
- 518 [15] Davidovits J. *Geopolymer chemistry and applications*. 3rd ed. France: Institut  
519 Géopolymère; 2011.
- 520 [16] Al Bakri Abdullah MM, Hussein K, Bnhussein M, Ismail KN, Yahya Z, Razak RA. Fly  
521 ash-based geopolymer lightweight concrete using foaming agent. *Int J Mol Sci* 2012; **13**:  
522 7186-98.
- 523 [17] Medpelli D, Seo J-M, Seo D-K. Geopolymer with hierarchically meso/macroporous  
524 structure from reactive emulsion templating. *J Am Ceram Soc* 2014; **97**: 70-3
- 525 [18] M.S. Cilla, M.R. Morelli, P. Colombo, Open cell geopolymer foams by a novel  
526 saponification/peroxide/gelcasting combined route, *J Eur Ceram Soc* 34 (2014) 3133-  
527 3137.
- 528 [19] Nakamura T, Gnyloskurenko SV, Sakamoto K, Byakova AV, Ishikawa R. Development  
529 of new foaming agent for metal foam. *Mater Trans* 2002; **43**: 1191-6.
- 530 [20] Fernandes HR, Tulyaganov DU, Ferreira JMF. Preparation and characterization of  
531 foams from sheet glass and fly ash using carbonates as foaming agents. *Ceram Int* 2009;  
532 **35**: 229-35.
- 533 [21] Yoshino A, Iwami I. Inorganic foam and preparation thereof. U.S. Patent 4,207,113,  
534 June 10 1980.

- 535 [22] Li SH, De Wijn JR, Layrolle P, de Groot K. Synthesis of macroporous hydroxyapatite  
536 scaffolds for bone tissue engineering. *J Biomed Mater Res* 2002; **61**: 109-20.
- 537 [23] Liu LP, Cui XM, He Y, Liu SD, Gong SY. The phase evolution of phosphoric acid-based  
538 geopolymers at elevated temperatures. *Mater Lett* 2012; **66**: 10-2.
- 539 [24] TM C329-88, Standard Test Method for Specific Gravity of Fired Ceramic Whiteware  
540 Materials, Annual Book of ASTM Standards, 1988.
- 541 [25] Larson AC, Von Dreele RB. GSAS Generalized structure analysis system. Laur 86-748.  
542 Los Alamos: Los Alamos National Laboratory; 1994.
- 543 [26] Toby BH. EXPGUI, a graphical user interface for GSAS. *J Appl Crystallogr* 2001; **34**:  
544 210-13.
- 545 [27] Lassinantti Gualtieri M, Romagnoli M, Miselli P, Cannio M, Gualtieri AF. Full  
546 quantitative phase analysis of hydrated lime using the Rietveld method. *Cem Concr Res*  
547 2012; **42**: 1273-9.
- 548 [28] Gualtieri AF. Accuracy of XRPD QPA using the combined Rietveld-RIR method. *J*  
549 *Appl Crystallogr* 2000; **33**: 267-78.
- 550 [29] Swenson CA. Recommended values for the thermal expansivity of silicon from 0 to 1000  
551 K. *J Phys Chem Ref Data* 1983; **12**: 179-82.
- 552 [30] Ishizawa N, Miyata T, Minatio I, Marumo F, Iwai S. A structural investigation of  $\alpha$ -  
553  $\text{Al}_2\text{O}_3$  at 2170 K. *Acta Crystallogr* 1980; **B36**: 228-30.
- 554 [31] Graetsch H. Two forms of aluminium phosphate tridymite from X-ray powder data. *Acta*  
555 *Crystallogr* 2000; **C56**: 401-3.
- 556 [32] Dows RT, Palmer DC. The pressure behaviour of alpha cristobalite. *Am Mineral* 1994;  
557 **79**: 9-14
- 558 [33] Wycoff RWG. Die Kristallstruktur von  $\beta$ -Cristobalit  $\text{SiO}_2$  (bei hohen Temperaturen  
559 stabile Form). *Z Kristallogr* 1925; **62**: 189-200.

- 560 [34] Le Page Y, Donnay G. Refinement of the crystal structure of low-quartz. *Acta Cryst*  
561 1976; **B32**: 2456-7.
- 562 [35] Popovic J, Tkalcec E, Grzeta B, Kurajica S, Schmauch J. Cobalt incorporation in mullite,  
563 *Am Mineral* 2007; **92**: 408-11.
- 564 [36] Graetsch HA, Hexagonal high-temperature form of aluminium phosphate tridymite from  
565 X-ray powder data, *Acta Crystallogr* 2001; **C57**: 665-7.
- 566 [37] Pryde AKA, Dove MT. On the sequence of phase transitions in tridymite. *Phys Chem*  
567 *Mineral* 1998; **26**: 171-9.
- 568 [38] Nukui A, Nakazawa H, Akao M. Thermal changes in monoclinic tridymite. *Am Mineral*  
569 1978; **63**: 1252-59.
- 570 [39] Gualtieri A, Bellotto M. Modelling the structure of metastable phases in the reaction  
571 sequence kaolinite-mullite by X-ray scattering experiments. *Phys Chem Minerals* 1998;  
572 **25**: 442-52.
- 573 [40] Collins TJ. ImageJ for microscopy. *Biotechniques* 2007;**43**: 25-30.
- 574 [41] Washburn EW. The dynamics of capillary flow. *Phys Rev* 1921;**17**: 273-83.
- 575 [42] Lassinantti Gualtieri M, Romagnoli M, Pollastri S, Gualtieri AF. Inorganic polymers  
576 from laterite using activation with phosphoric acid and alkaline sodium silicate solution:  
577 mechanical and microstructural properties. *Cem Concr Res* 2015; **67**: 259-70.
- 578 [43] Duval DJ, Risbud SH, Shackelford JF. Mullite. In: Shackelford JF, Doremus RH,  
579 editors. *Ceramic and glass materials: Structure, properties and processing*, New York:  
580 Springer Science+Business Media; 2008, p. 27-38.
- 581 [44] Ban T, Okada K. Structure refinement of mullite by the Rietveld method and a new  
582 method for estimation of chemical composition. *J Am Ceram Soc* 1992; **75**: 227-30.
- 583 [45] Mooney RCL. The crystal structure of aluminum phosphate and gallium phosphate, low-  
584 cristobalite type. *Acta Crystallogr* 1956; **9**: 728-34.

- 585 [46] Graetsch HA. Thermal expansion and thermally induced variations of the crystal  
586 structure of  $\text{AlPO}_4$  low cristobalite. *N Jb Miner Mh* 2003; **7**: 289-301.
- 587 [47] Horn WF, Hummel FA. Axial thermal expansion of cristobalite  $\text{AlPO}_4$  and related  
588 cristobalite solid solution phases. *J Am Ceram Soc* 1980; **63**: 338-9.
- 589 [48] Wright AF, Leadbetter AJ. The structures of the  $\beta$ -cristobalite phases of  $\text{SiO}_2$  and  $\text{AlPO}_4$ ,  
590 *Philos Mag* 1975; **31**: 1391-401.
- 591 [49] Leadbetter AJ, Wright AF. The  $\alpha$ - $\beta$  transition in the cristobalite phases of  $\text{SiO}_2$  and  
592  $\text{AlPO}_4$  I. X-ray studies. *Philos Mag* 1976; **33**: 105-12.
- 593 [50] Thomas ES, Thompson JG, Withers RL, Sterns M, Xiao Y, Kirkpatrick RJ. Further  
594 Investigation of the Stabilization of  $\beta$ -Cristobalite. *J Am Ceram Soc* 1994; **77**: 49-56.
- 595 [51] Graetsch H. X-ray powder diffraction study of the modulated high temperature forms of  
596  $\text{SiO}_2$  tridymite between 110 and 220 °C. *Phys Chem Mineral* 2001; **28**: 313-21.
- 597 [52] Ackermann RJ, Sorrel CA. Thermal expansion and the High-Low transformation in  
598 quartz. I. High-temperature X-ray studies. *J Appl Crystallogr* 1974; **7**: 461-7.
- 599  
600  
601

## TABLES

Table 1. Composition of investigated base pastes, according to a 2 level factorial design with 5 centerpoints.

Sample	* wt.% deflocculant	MK/H <sub>2</sub> O	MK/H <sub>3</sub> PO <sub>4</sub>	Weight composition					
				deflocculant	H <sub>3</sub> PO <sub>4</sub> (85 wt.%)	H <sub>2</sub> O	MK	lime stone	surfactant
1	0	1.2	2.0	0	53.5	75.3	100	4	0.16
2	0.5	1.2	2.0	0.5	53.5	75.3	100	4	0.16
3	0	1.4	2.0	0	53.5	63.4	100	4	0.16
4	0.5	1.4	2.0	0.5	53.5	63.4	100	4	0.16
5	0	1.2	3.8	0	26.7	79.3	100	4	0.16
6	0.5	1.2	3.8	0.5	26.7	79.3	100	4	0.16
7	0	1.4	3.8	0	26.7	67.4	100	4	0.16
8	0.5	1.4	3.8	0.5	26.7	67.4	100	4	0.16
9	0.25	1.3	2.9	0.25	35.6	71.6	100	4	0.16
10	0.25	1.3	2.9	0.25	35.6	71.6	100	4	0.16
11	0.25	1.3	2.9	0.25	35.6	71.6	100	4	0.16
12	0.25	1.3	2.9	0.25	35.6	71.6	100	4	0.16
13	0.25	1.3	2.9	0.25	35.6	71.6	100	4	0.16

\*with respect to MK

**Table 2.** Chemical and mineralogical composition, determined by XRF and FQPA, of industrial metakaolin used for sample preparation.

Chemical composition (wt.%)										
SiO <sub>2</sub>	Al <sub>2</sub> O <sub>3</sub>	Fe <sub>2</sub> O <sub>3</sub>	TiO <sub>2</sub>	MgO	K <sub>2</sub> O	CaO	Cr <sub>2</sub> O <sub>3</sub>	Na <sub>2</sub> O	MnO	L.O.I.
59.45	37.24	0.77	0.46	0.51	1.02	0.42	0.01	0.67	0.01	1.3
*Mineralogical composition (wt.%)										
quartz		muscovite/illite			microcline			amorphous		
13.2 ± 0.3		4.5 ± 0.2			0.7 ± 0.1			81.6 ± 0.4		

\*Anatase and hematite in trace amounts (< 0.5%)

**Table 3.** Various macroscopic properties ( $\rho_t$ =true density,  $\rho$  = bulk density, TP= total porosity, TC=thermal conductivity) of as-prepared samples based on the paste compositions presented in Table 2.

Sample	$\rho_t$ (g/cm <sup>3</sup> )	$\rho$ (g/cm <sup>3</sup> )	TP (%)	TC (W/mK)
1	2.323±0.002	0.60±0.06	74±2	0.08±0.02
2	2.290±0.004	0.6±0.1	75±4	0.07±0.02
3	2.299±0.004	0.7±0.2	69±8	0.09±0.01
4	2.326±0.004	0.73±0.06	69±3	0.073±0.004
5	2.370±0.004	0.61±0.05	74±4	0.089±0.008
6	2.375±0.003	0.67±0.07	72±3	0.09±0.01
7	2.373±0.004	0.67±0.07	72±3	0.090±0.007
8	2.388±0.005	0.6±0.1	74±4	0.08±0.01
9	2.351±0.004	0.58±0.05	76±2	0.08±0.02
10	2.337±0.004	0.70±0.05	70±2	0.091±0.005
11	2.355±0.002	0.63±0.05	72±2	0.07±0.01
12	2.355±0.005	0.6±0.1	73±5	0.09±0.03
13	2.334±0.004	0.6±0.1	73±5	0.08±0.01

**Table 4.** FQPA results for each investigated composition following calcination at 1000 °C

for 3h.

Sample	Mineralogical composition (wt.%)					
	tridymite-type	cristobalite-type	mullite	quartz	whitlockite	amorphous
1	19.4±0.3	37.1±0.3	11.2±0.4	11.2±0.4	0.97±0.09	25.1±0.6
2	30.0±0.4	30.2±0.4	12.6±0.6	8.5±0.1	*	18.4±0.8
3	24.9±0.5	32.2±0.5	13.3±0.4	7.7±0.2	0.3±0.1	21.2±0.9
4	25.3±0.3	33.0±0.3	14.0±0.5	7.2±0.1	1.1±0.1	11.6±0.4
5	22.7±0.3	25.3±0.3	24.0±0.3	7.5±0.1	*	20.6±0.5
6	23.9±0.3	22.4±0.3	23.7±0.3	8.4±0.1	*	21.5±0.5
7	20.2±0.3	22.1±0.2	22.1±0.3	8.3±0.1	0.34±0.08	27.0±0.5
8	16.9±0.3	27.8±0.4	21.8±0.4	5.7±0.1	0.68±0.08	27.2±0.7
9	21.6±0.4	26.8±0.5	20.8±0.4	7.5±0.2	1.5±0.1	21.7±0.8
10	23.2±0.4	25.6±0.4	18.2±0.4	8.6±0.2	0.5±0.1	24.0±0.7
11	23.8±0.4	25.1±0.4	16.3±0.4	7.7±0.1	0.35±0.08	26.7±0.7
12	23.2±0.4	22.2±0.4	16.0.2±0.4	9.0±0.1	*	29.6±0.7
13	25.7±0.3	23.0±0.2	17.3±0.3	8.8±0.1	1.3±0.1	23.8±0.5

\*&lt;0.3 wt%

**Table 5.** Results from XRF analyses of each composition following calcination at 1000 °C for 3h

Chemical composition (Wt.%)											
	SiO <sub>2</sub>	Al <sub>2</sub> O <sub>3</sub>	P <sub>2</sub> O <sub>5</sub>	Na <sub>2</sub> O	CaO	MgO	K <sub>2</sub> O	Fe <sub>2</sub> O <sub>3</sub>	TiO <sub>2</sub>	SO <sub>3</sub>	Cr <sub>2</sub> O <sub>3</sub>
1	42.54	26.13	24.07	2.46	2.23	0.71	0.70	0.52	0.50	0.11	0.01
2	42.60	26.25	24.48	2.69	1.57	0.67	0.77	0.52	0.32	0.08	0.01
3	43.41	26.01	26.12	0.98	1.63	0.03	0.71	0.52	0.36	-	0.01
4	41.44	26.27	25.26	2.31	2.33	0.67	0.77	0.52	0.31	0.09	0.01
5	48.17	30.50	15.83	1.54	1.39	0.65	0.83	0.60	0.37	0.1	0.01
6	48.36	29.88	15.87	1.91	1.60	0.54	0.83	0.60	0.37	0.02	0.01
7	48.06	29.85	15.49	1.80	1.85	0.71	0.77	0.59	0.52	0.05	0.01
8	47.43	28.99	15.85	2.87	2.30	0.71	0.85	0.57	0.41	-	0.01
9	45.36	28.38	18.66	2.53	2.58	0.70	0.85	0.56	0.34	-	0.01
10	45.17	28.28	19.17	3.16	1.89	0.61	0.85	0.57	0.34	-	0.01
11	45.90	27.87	19.22	2.77	1.79	0.56	0.78	0.57	0.54	-	0.01
12	45.99	28.44	19.00	2.57	1.62	0.61	0.82	0.58	0.40	-	0.01
13	45.42	28.50	19.27	2.06	2.30	0.70	0.80	0.57	0.35	-	0.01

## FIGURE CAPTIONS

**Fig.1.** XRD patterns for metakaolin used as raw material for sample preparation (a) as well as the natural limestone used as pore forming agent (b).

**Fig. 2.** Low-magnification BSE images of polished cross-sections of samples having compositions 10 (a) and 3 (b).

**Fig. 3.** The Rietveld refinement output of an as-prepared sample having composition 3. The observed, calculated and difference curve are depicted. The tickmarks indicate the following phases starting from the top: quartz, muscovite/illite, tridymite, corundum (NIST 676a).

**Fig. 4.** The results obtained for various properties of the heat-treated foams as a function of the corresponding values obtained for as-prepared samples: (a) true density  $\rho_t$ , (b) bulk density  $\rho$ , (c) Total porosity TP, (d) Thermal conductivity TC.

**Fig. 5.**  $dV/d\log D$  ( $V$  =volume of intruded mercury) and the cumulative pore volume (indicated by arrows) as a function of pore diameter ( $D$ ) for specimens with sample compositions 3 (a) and 10 (b). Data for both as-prepared (continuous line) and calcined (1000°C, dotted line) samples are depicted.

**Fig. 6.** Results of the thermogravimetric analysis of a powder obtained from a sample having composition 3.

**Fig. 7.** *in-situ* XRPD data (650-960 °C) collected for a sample having composition 3. The insert shows the FQPA results in which the known amount of intrinsic quartz was used as internal standard.

**Fig. 8.** XRPD patterns for specimens obtained by calcination of a sample having composition 3. The duration of the heat-treatment was 3h and the investigated temperatures were 800, 900 and 1000 °C.

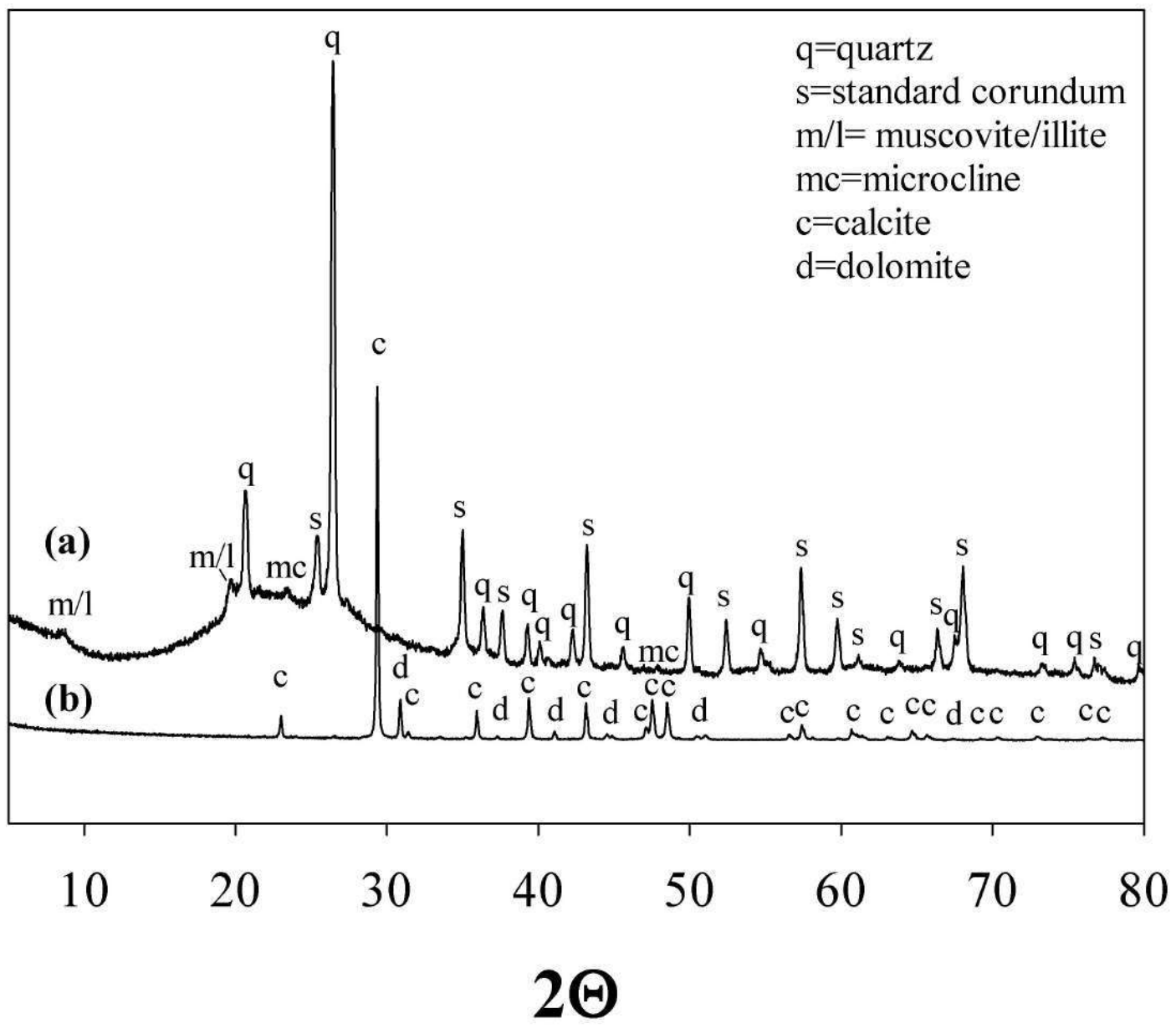
**Fig. 9.** Wt.% of major phases as a function of calcination temperature for composition 3.

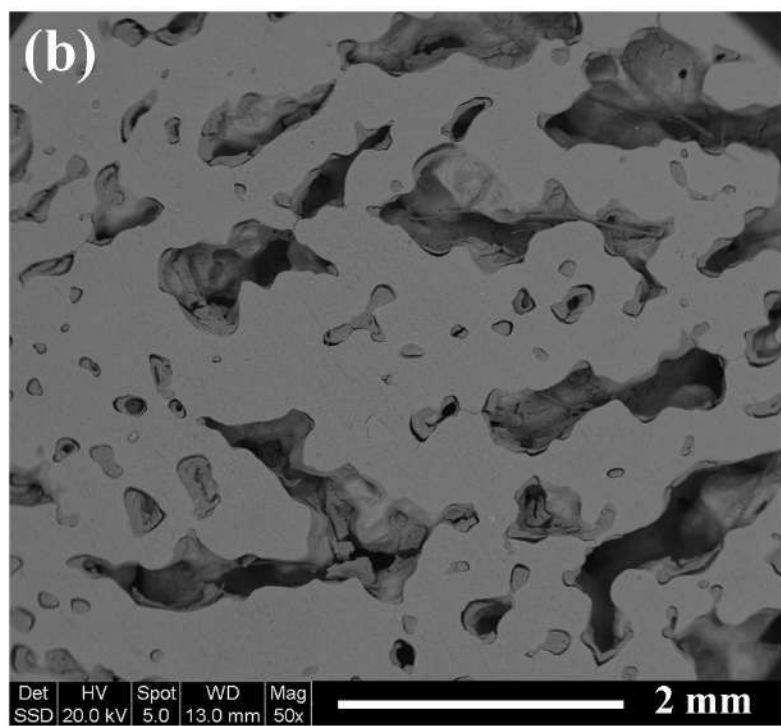
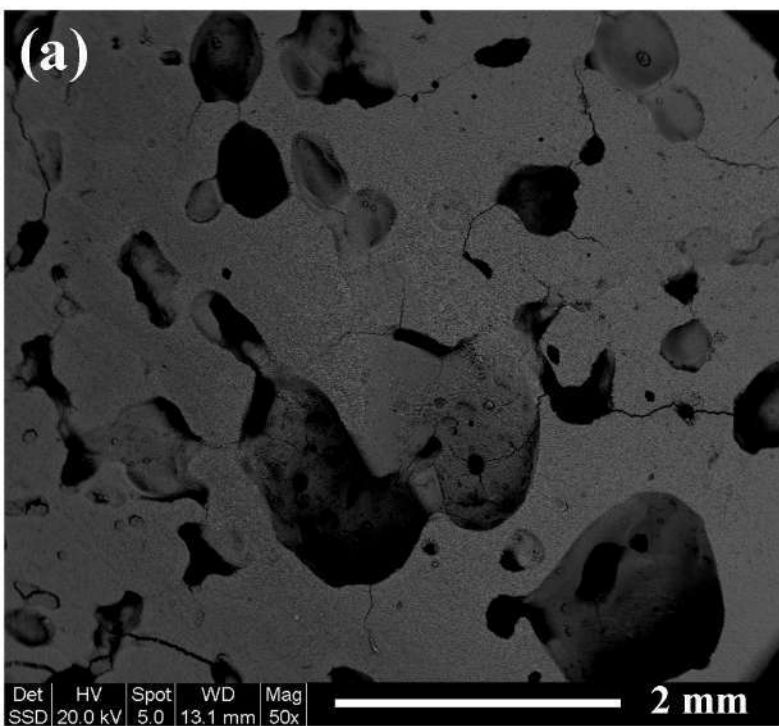
**Fig. 10.** TEM images of a calcined (1000°C) specimen having composition 3. Results from EDS spot analyses (molar composition, oxygen excluded) are reported. See text for definition of symbols (A,B,C,D).

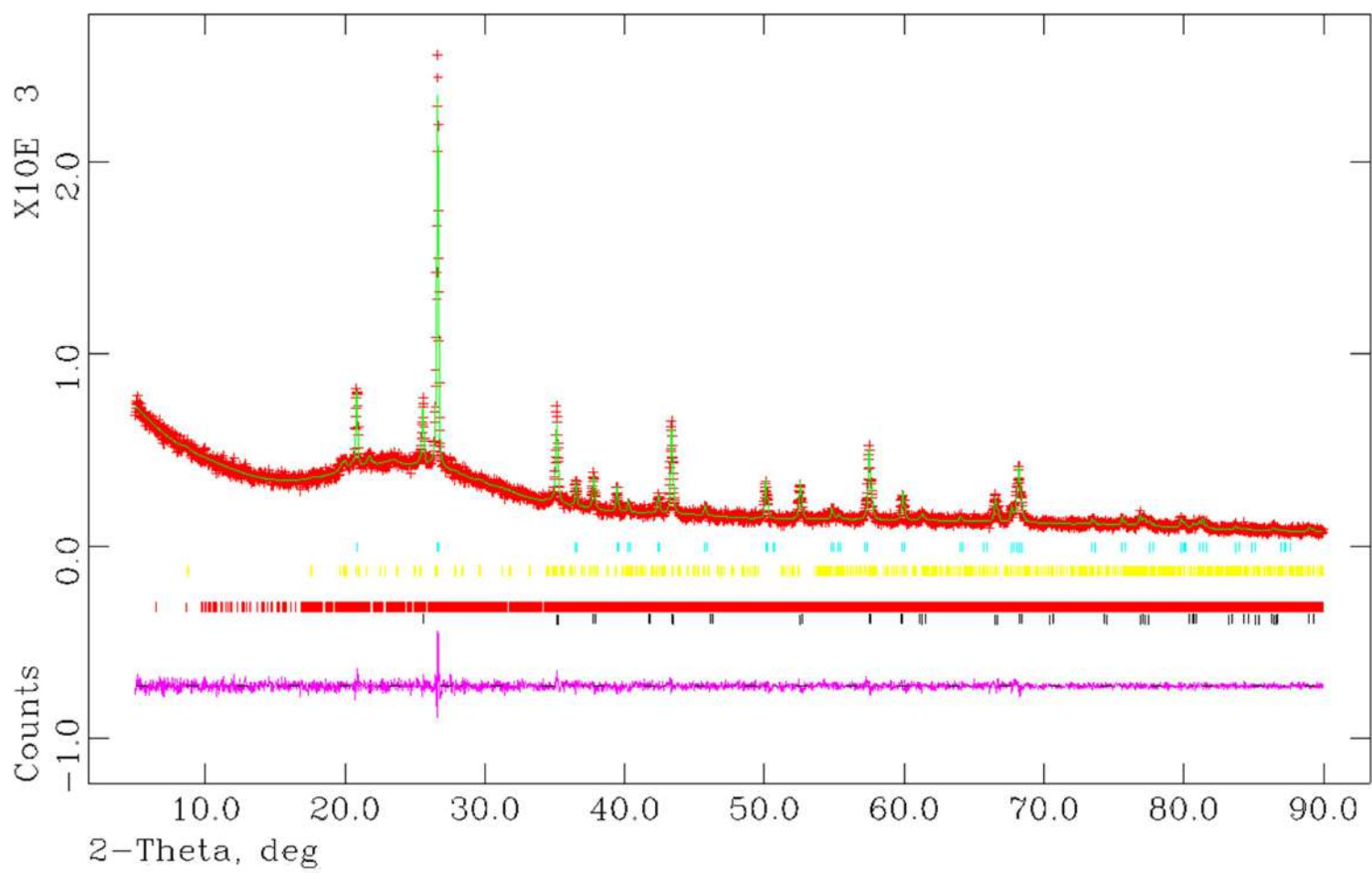
**Fig. 11a.** Unit cell volume of cristobalite as a function of temperature (*in situ* data) for a sample (composition 3) precalcined at 800 °C and 1000 °C. Literature data for  $\text{AlPO}_4\text{-SiO}_2$  and  $\text{SiO}_2\text{-AlPO}_4$  cristobalite solid solutions are also shown for comparison.

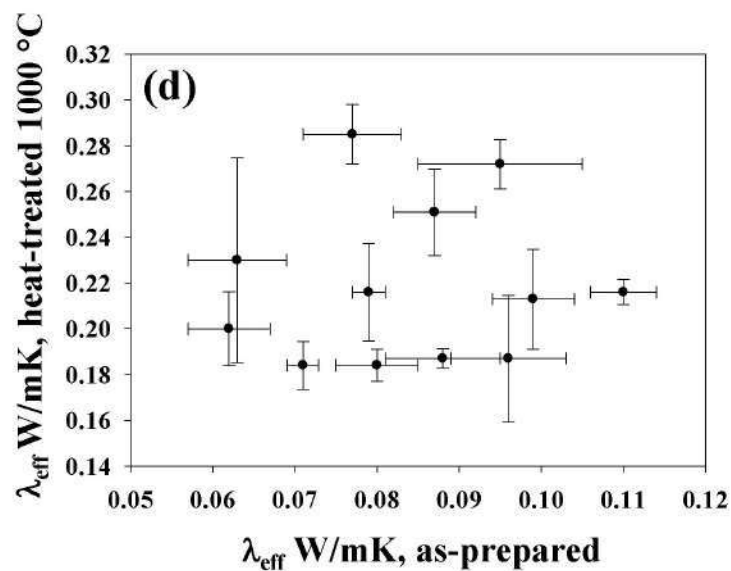
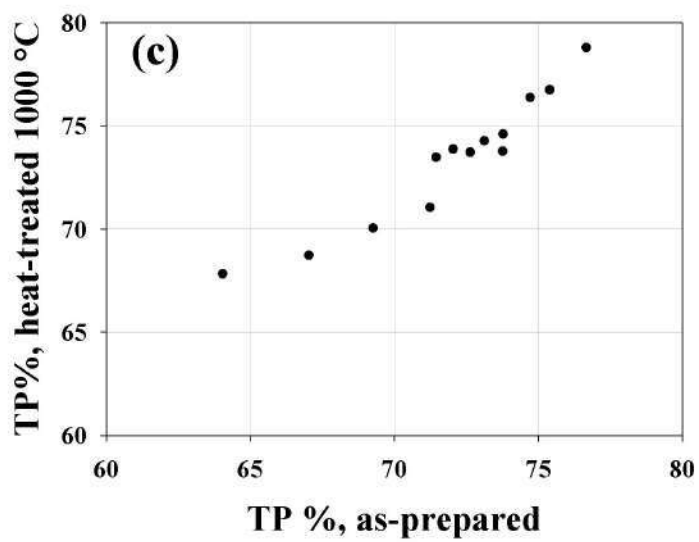
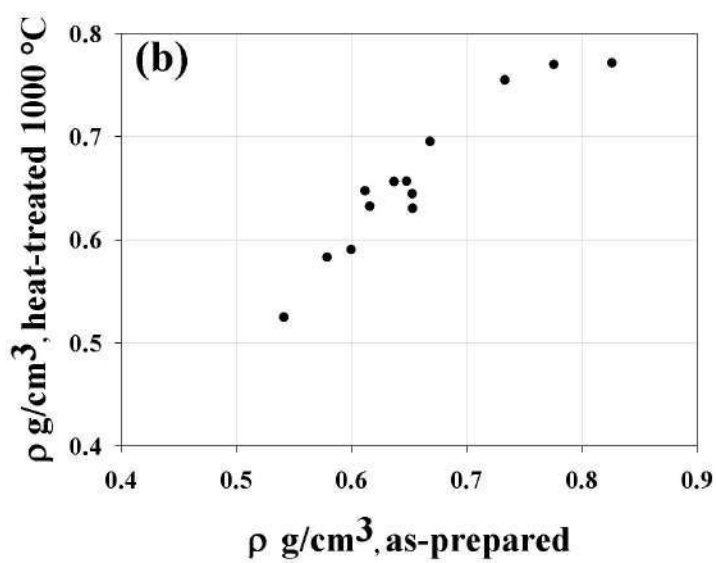
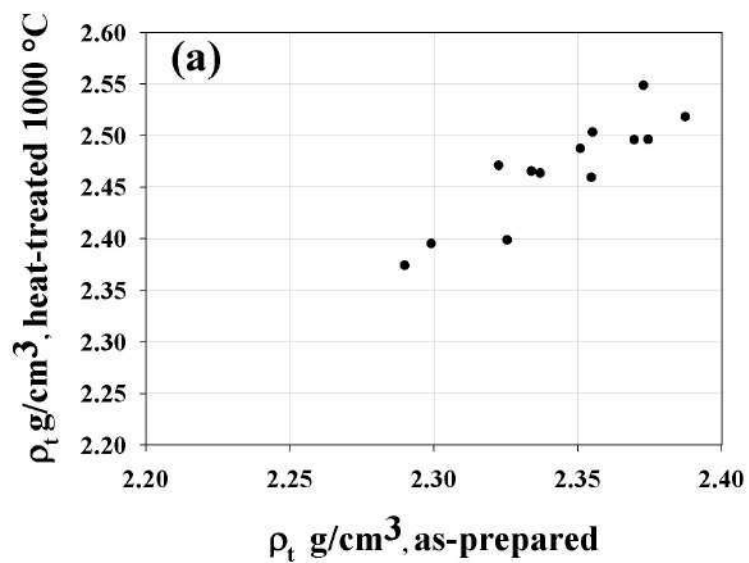
**Fig. 11b.** Unit cell volume of tridymite (triclinic, space group  $F1 [31]$ ) and quartz as a function of temperature (*in situ* data) for a sample (composition 3) precalcined at 800 °C and 1000 °C.

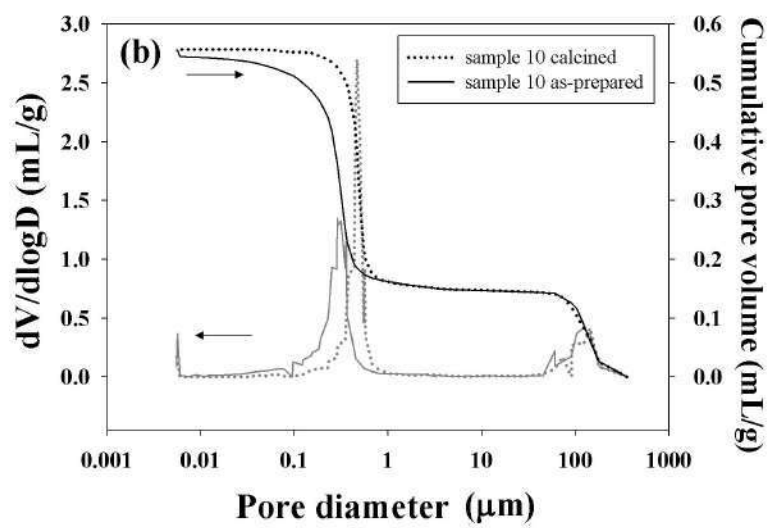
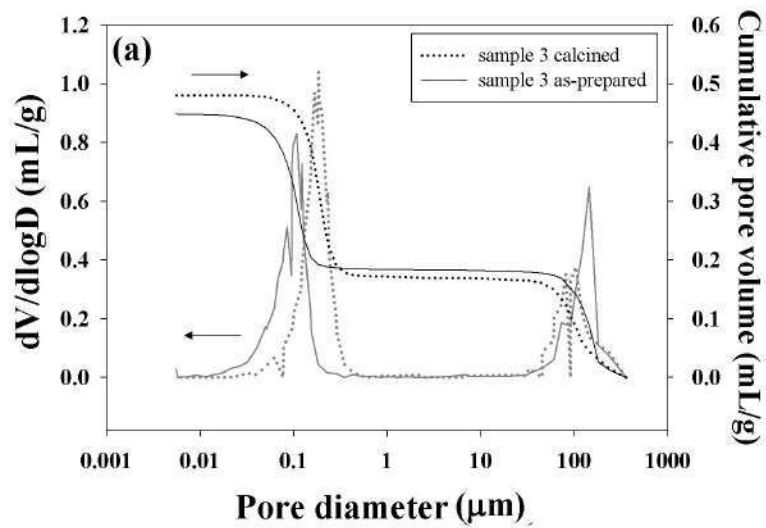
Intensity (a.u.)

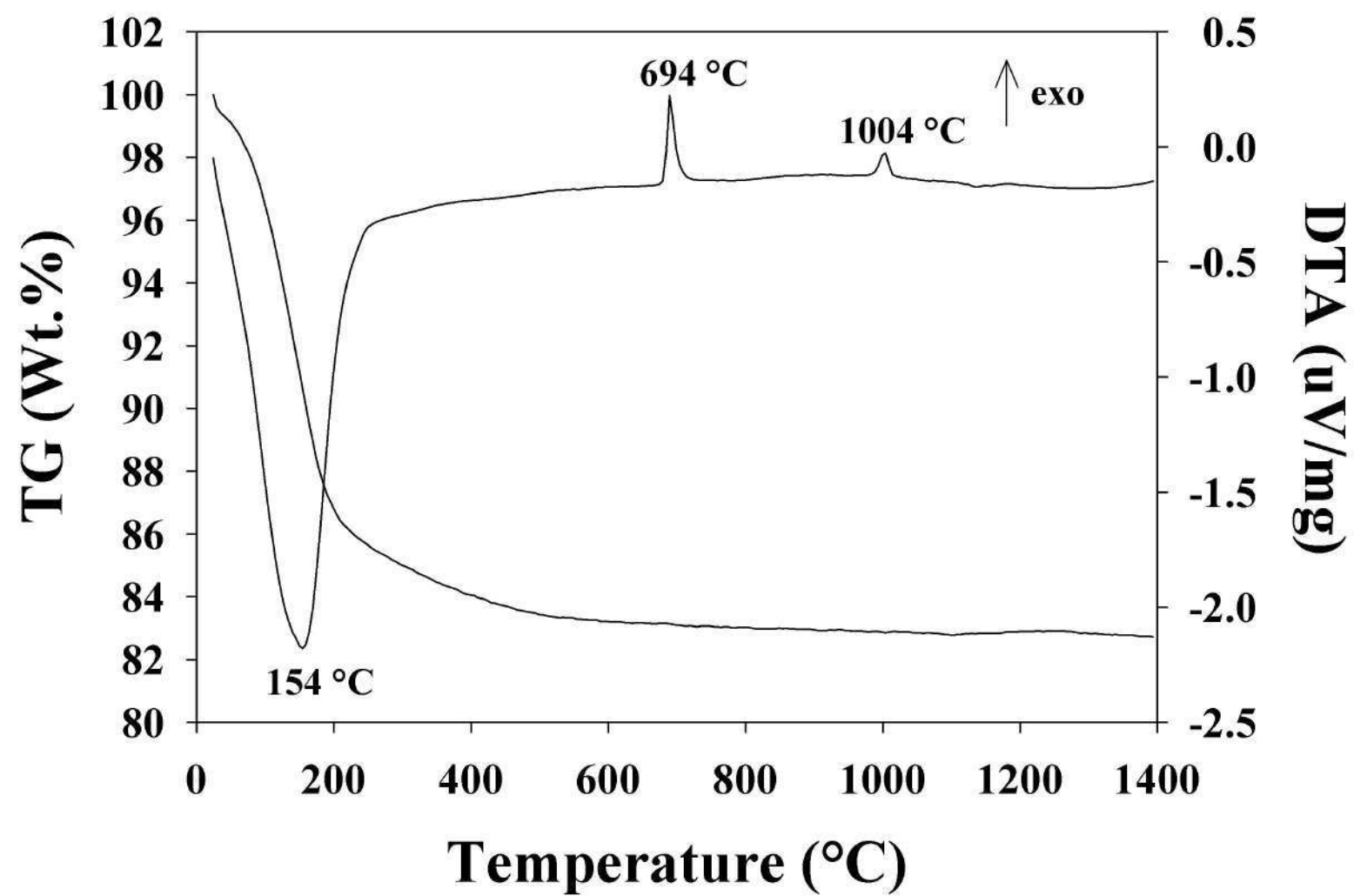


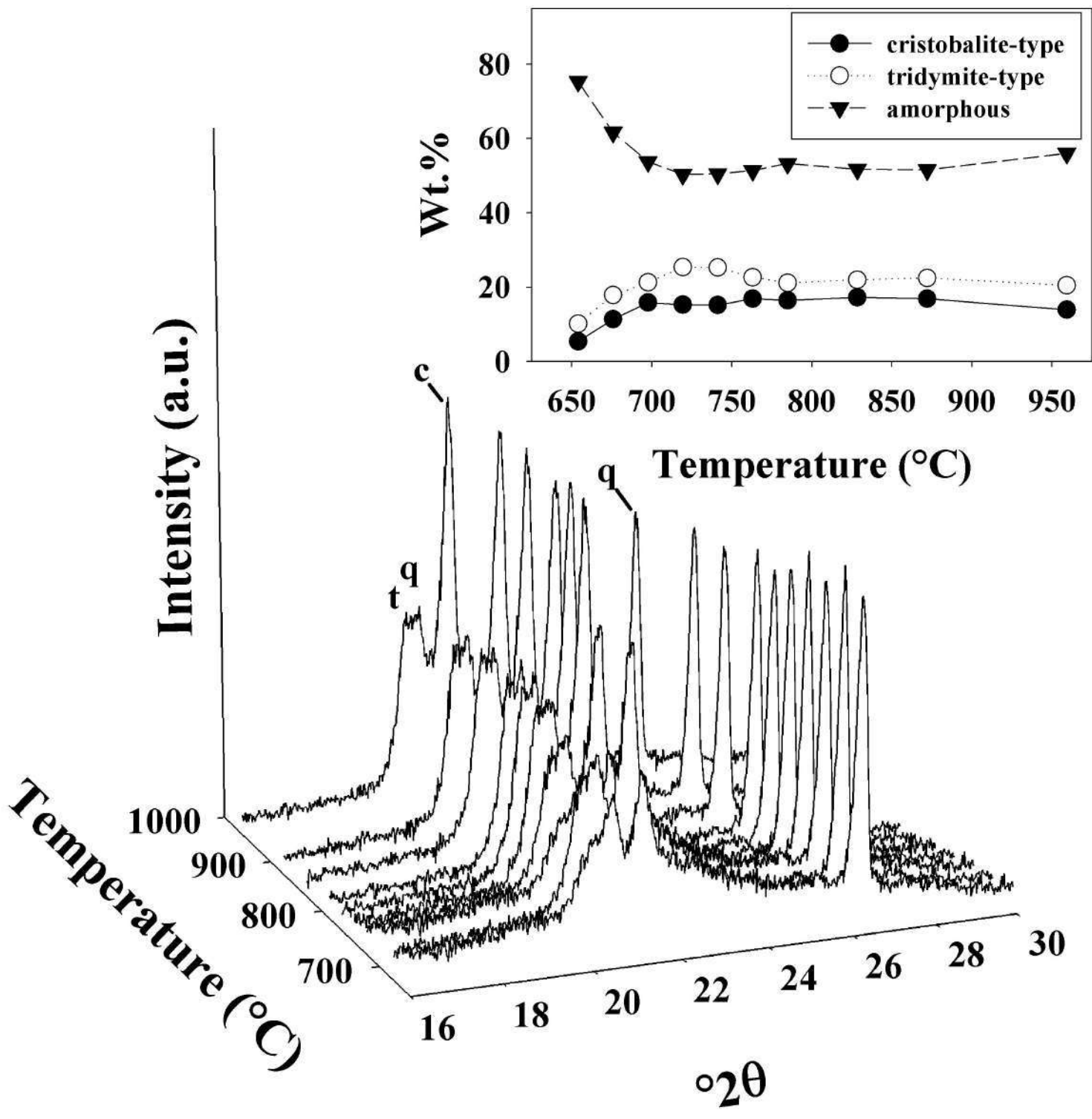












Intensity (a.u.)

